Effects of wavelength and amplitude of a wavy cylinder in cross-flow at low Reynolds numbers

K. LAM† AND Y. F. LIN

Department of Mechanical Engineering, The Hong Kong Polytechnic University,
Hung Hom, Kowloon, Hong Kong

Three-dimensional numerical simulations of laminar flow around a circular cylinder with sinusoidal variation of cross-section along the spanwise direction, named 'wavy cylinder', are performed. A series of wavy cylinders with different combinations of dimensionless wavelength (λ/D_m) and wave amplitude (a/D_m) are studied in detail at a Reynolds number of $Re = U_\infty D_m/\nu = 100$, where U_∞ is the free-stream velocity and D_m is the mean diameter of a wavy cylinder. The results of variation of mean drag coefficient and root mean square (r.m.s.) lift coefficient with dimensionless wavelength show that significant reduction of mean and fluctuating force coefficients occurs at optimal dimensionless wavelengths λ/D_m of around 2.5 and 6 respectively for the different amplitudes studied. Based on the variation of flow structures and force characteristics, the dimensionless wavelength from $\lambda/D_m = 1$ to $\lambda/D_m = 10$ is classified into three wavelength regimes corresponding to three types of wake structures. The wake structures at the near wake of different wavy cylinders are captured. For all wavy cylinders, the flow separation line varies along the spanwise direction. This leads to the development of a three-dimensional free shear layer with periodic repetition along the spanwise direction. The three-dimensional free shear layer of the wavy cylinder is larger and more stable than that of the circular cylinder, and in some cases the free shear layer even does not roll up into a mature vortex street behind the cylinder. As a result, the mean drag coefficients of some of the typical wavy cylinders are less than that of a corresponding circular cylinder with a maximum drag coefficient reduction up to 18 %. The r.m.s. lift coefficients are greatly reduced to practically zero at optimal wavelengths. In the laminar flow regime ($60 \leqslant Re \leqslant 150$), the values of optimal wavelength are Reynolds number dependent.

1. Introduction

Flows past bluff bodies are important in many engineering applications, for example in the designs for heat exchangers, offshore structures, high-rise buildings, chimneys, and cables. The periodic vortex shedding and fluctuating velocity fields behind the bluff bodies can cause structural damage as a result of periodic surface loading which increases the vibration of the bodies and shortens the life of the structures. In fundamental research, flow past cylindrical bodies has been extensively investigated. It is a challenge to control the vortex-shedding phenomenon and hence to reduce the potential for flow-induced vibration (FIV). Over the past years, many experimental and numerical investigations had been carried out on the control of FIV of the

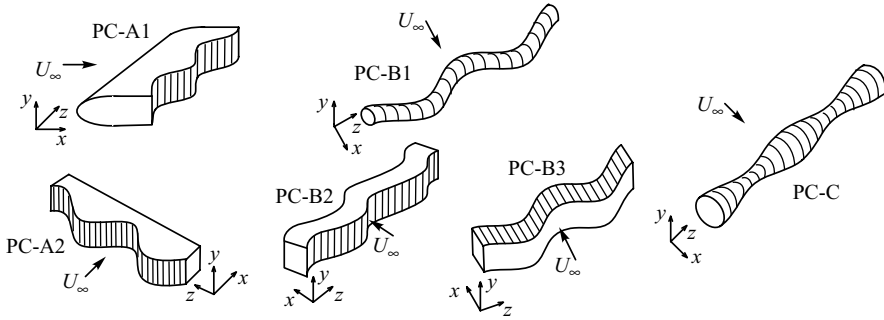† Email address for correspondence: mmklam@polyu.edu.hk

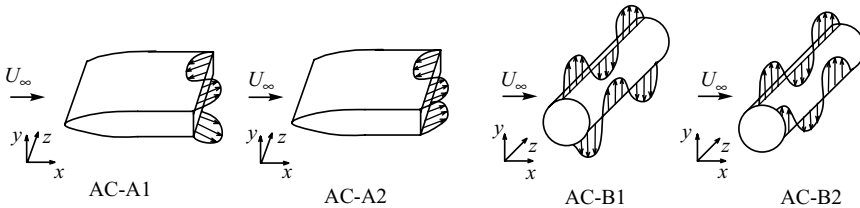FIGURE 1. Simple model types for different wavy cylinders.

FIGURE 2. Simple model types for active control of the flow induced vibrations.

cylindrical structures. It is well known that the free shear layers generated by bluff bodies have a profound influence on the wake structure and hence on the force characteristic of the bluff body. In the recent few years, several types of cylinders with surface profile varying sinusoidally along their spanwise direction, named wavy cylinders, were introduced (see figure 1). Ahmed & Bays-Muchmore (1992), Ahmed, Khan & Bays-Muchmore (1993), Tombazis & Bearman (1997), Bearman & Owen (1998), Owen, Szewczyk & Bearman (2000), Darekar & Sherwin (2001*a*, *b*), Keser *et al.* (2001), Lam *et al.* (2004), Lam, Wang & So (2004), Zhang, Dai & Lee (2005), Dobre, Hangan & Vickery (2006), Lee & Nguyen (2007) and Lam & Lin (2007, 2008) have investigated various types of wavy objects experimentally and numerically under different flow conditions. Their studies are summarized in table 1.

Tombazis & Bearman (1997) introduced a spanwise wavy surface to the trailing face of the cylindrical bodies (figure 1; PC-A1), while Bearman & Owen (1998) and Dobre *et al.* (2006) investigated the effects of a spanwise wavy surface at the leading face (figure 1; PC-A2) of the cylindrical bodies. At Reynolds number $Re = 40\,000$, the maximum drag reduction of about 30 % was obtained by Bearman & Owen (1998). Owen *et al.* (2000) studied flow past a sinuous bluff body (figure 1; PC-B1), using flow visualization method and found that the Kármán vortex shedding was effectively suppressed, and a periodic variation in the wake width across the spanwise direction was observed. Darekar & Sherwin (2001*a*, *b*) numerically investigated the flow past a square cylinder with a wavy stagnation face at low Reynolds numbers (figure 1; PC-B2, PC-B3). They showed that the unsteady and staggered Kármán vortex wake could be suppressed to a steady and symmetric wake structure due to the waviness of the square cylinder. The maximum drag reduction of about 16 % was obtained at a Reynolds number of 100 compared with the straight, non-wavy square cylinder. Moreover, at higher Reynolds numbers, the drag reduction increases substantially.

Furthermore, active flow control method based on the idea of wavy surface effect is also pursued (see figure 2 and table 1). Kim *et al.* (2004) and Kim & Choi (2005) used

Authors	Types	Cross-section	Key features	*Re*	Methods
AC					
Kim *et al.* (2004)	AC-A1, A2	Half-ellipse shape	Three-dimensional vortex structures; Drag reduction	4200, 20 000–40 000	Num., Exp.
Kim & Choi (2005)	AC-B1, B2	Circular shape	Optimal regime of wave parameters	40–300, 3900	Num.
PC					
Tombazis & Bearman (1997)	PC-A1	Half-ellipse shape	Shedding frequency, wake patterns	2500, 40 000	Exp.
Bearman & Owen (1998)	PC-A2	Square shape	Drag reduction; wake stability	100, 40 000	Exp.
Dobre *et al.* (2006)	PC-A2	Square shape	Drag reduction	23500	Exp.
Owen *et al.* (2000)	PC-B1	Circular shape	Vortex shedding suppression	100	Exp.
Keser *et al.* (2001)	PC-B1, C	Circular shape	Three-dimensional vortex structures	NA	Num.
Darekar & Sherwin (2001*a, b*)	PC-B2, B3	Square shape	Optimal regime of wave parameters	10–200, 500	Num.
Ahmed & Bay-Muchmore (1992)	PC-C	Circular shape	Three-dimensional separation line, wake	5000–20 000	Exp.
Ahmed *et al.* (1993)	PC-C	Circular shape	topology Wake patterns	5000–20 000	Exp.
Lam *et al.* (2004*a, b*)	PC-C	Circular shape	Drag reduction; wake patterns	200–50 000	Exp.
Zhang *et al.* (2005)	PC-C	Circular shape	Periodic spanwise wake patterns	3000	Exp.
Lee & Nguyen (2007)	PC-C	Circular shape	Drag reduction	5000–20 000	Exp.
Lam & Lin (2007,2008)	PC-C	Circular shape	Drag reduction; three-dimensional vortex structures	100, 3000	Num.
Present study	PC-C	Circular shape	Optimal regime of wave parameters	60–150	Num.

TABLE 1. Summary of types of the wavy cylinder for the control of FIV: AC = active control; PC = passive control; Exp. = experimental measurement; Num. = numerical simulation.

an active open-loop control method (called distributed forcing) for the reduction of drag of a half-ellipse–shaped body (figure 2; AC-A1, AC-A2) and a circular cylinder (figure 2; AC-B1, AC-B2), respectively. The forcing profile was achieved by sinusoidal variation of blowing and suction from slots on the upper and lower surfaces of the object in the spanwise direction. The Kármán vortex shedding was attenuated for both laminar flow condition and turbulent flow condition, and the drag was also reduced substantially. Moreover, the vortex shedding was significantly suppressed for some typical cases at $Re = 100$ (Kim & Choi 2005).

Alternatively, a cylinder whose diameter varied sinusoidally along its spanwise direction was studied (figure 1; PC-C). Such cylinder is omnidirectional to the free oncoming flow. In fundamental research, experimental measurements on the surface–pressure distributions of such wavy cylinders with different spanwise wavelengths were carried out by Ahmed & Bays-Muchmore (1992). They found that the separated flow structures near the geometric nodes are distinctly asymmetric for a large fraction of time, and the sectional drag coefficients at the geometric nodes are greater than that at the geometric saddle. Ahmed et al. (1993) further investigated experimentally the turbulent wake behind a wavy cylinder. They described the topology of the boundary layer separation lines and the subsequent three-dimensional development of turbulent structure of the wake. The formation of trailing streamwise vortices behind the nodal points of separation gives rise to a locally narrower wake, a rapid wake velocity recovery and a suppression of the turbulence development within the separated boundary layer. However, the phenomena of the drag reduction and suppression of lift fluctuating were not discussed. Keser et al. (2001) used a three-dimensional discrete vortex method to simulate the separated flow around wavy cylinders. Lam et al. (2004a) started to focus attention on the effects of different wavy cylinders on drag and lift reduction and the related effects on FIV. It was anticipated that such type of cylinder could lead to a better control of the vortex shedding and hence a better suppression of FIV by changing the geometric wavelength and wave amplitude of the cylinder. For constant values of wave amplitude, they found experimentally that with the value of wavelength ratio from 1.45 to 2.27, a large value of drag reduction up to 20 % can be obtained in subcritical Reynolds numbers range of 20 000–50 000. It was also found that the root mean square (r.m.s.) lift coefficients of the wavy cylinders are much lower than those of the circular cylinder. Furthermore, Lam et al. (2004b) measured the near wake velocity distributions of a wavy cylinder. They found that the wavy geometry played an important role in vortex formation length, drag reduction and vortex shedding suppression. The vortex formation length of the wavy cylinder is longer than that of the circular cylinder. Flow visualization studies were also performed, and in the near wake of the wavy cylinder, the rib structures were detected near the saddle planes at the Reynolds number of 600. At the nodal and saddle planes, the streamwise velocity distributions are very different compared with those of a circular cylinder. Recently, Zhang et al. (2005) investigated the three-dimensional near wake structures behind a wavy cylinder by using the particle image velocimetry (PIV) technique at the Reynolds number of 3000. Along the spanwise direction of the wavy cylinder, well-organized streamwise vortices with alternating positive and negative vortices were observed. They suppress the formation of the large-scale spanwise vortices and decrease the overall turbulent kinetic energy in the near wake of the wavy cylinder. Experiments by Lee & Nguyen (2007) and others, using hot-wire anemometer and flow visualization method, over a wide range of Reynolds number from 5300 to 50 000, showed that when the values of wavelength ratio equal 2, wavy cylinders can give rise to larger drag reductions

than when those ratios equal 1. The maximum drag reduction of up to 22 % is obtained at wavelength ratio of 2 and $Re = 10\,000$. They also showed that the longer vortex formation region of the wavy cylinder seems to be related to the effect of drag reduction. At similar Reynolds numbers, the vortex formation length is longer and the turbulent intensity smaller than those of the circular cylinder. From these results, it can be seen that an optimal value of spanwise wavelength ratio exists in the lower wavelength ratio range of 1–2.27 for drag reduction at higher Reynolds numbers. Recently, Lam & Lin (2007, 2008) carried out computational studies and captured the detailed three-dimensional vortex structures of wavy cylinders for laminar flow at low Reynolds number $Re = 100$ and in turbulent flow at $Re = 3000$; the optimal values of spanwise wavelength for drag reduction were obtained over a small range of wavelength variation. For turbulent flow, they confirmed the findings above by using the large eddy simulation for wavy cylinders with wavelength ratio of 1.14–3.33 at $Re = 3000$. The optimal value of wavelength ratio for turbulent flow was around $\lambda/D_m = 1.9$. The relationships between the vortex formation length and drag were also given.

All investigations above with respect to the wavy cylinder of model type PC-C (figure 1) have only been performed over a small region of the wavelength ratio λ/D_m along the spanwise direction. The optimal value of wavelength which can well control the vortex formation is still not fully revealed over a wider range of wavelength ratio. The amplitude ratio a/D_m of the wavy cylinder should also play an important role in the control of the vortex structure from the wavy cylinders. The aim of the present work is to apply a well-established three-dimensional numerical simulation method to carry out extensive investigations on laminar flows past wavy cylinders. It is anticipated that numerical simulations can well capture the instantaneous three-dimensional vortex structures and other valuable data, such as drag, lift, pressure and vortex shedding frequency and thus provide a fuller picture for the understanding of the complex flow phenomenon. The relationship between wavelength, wave amplitude and force reduction can be fully investigated, and the effect of Reynolds number can also be examined.

2. Parametric definition of the body geometry

As shown in figure 3, the diameter of the wavy cylinder varies sinusoidally along its spanwise direction. The geometry of the wavy cylinders is described by the following equation:

$$D_z = D_m + 2a\cos(2\pi z/\lambda), \qquad (2.1)$$

where D_z denotes the local diameter of the wavy cylinder and varies in the spanwise direction z. The mean diameter D_m is defined by

$$D_m = (D_{min} + D_{max})/2. \qquad (2.2)$$

The amplitude of the wavy surface a is equal to half peak-to-peak distance. The spanwise wavelength λ is also indicated in figure 3. The axial location with maximum local diameter D_{max} is called 'node', while the axial location of the minimum diameter D_{min} is called 'saddle'. The 'middle' is also defined at the midpoint position between nodal and saddle planes. The diameter of the middle cross-section is equal to the mean diameter D_m. The nodal position of the wavy cylinder along the spanwise direction is denoted by $z/\lambda = 0$, while $z/\lambda = 0.5$ denotes the saddle position. Furthermore, a
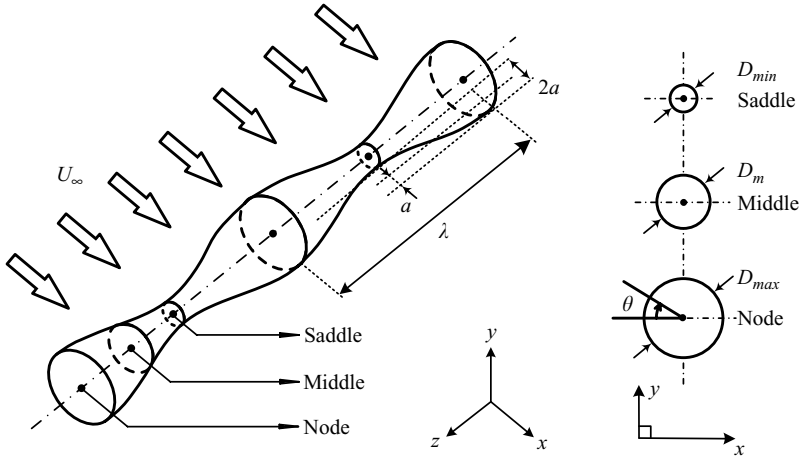
FIGURE 3. Schematic diagram of a wavy cylinder.

circular cylinder with diameter D_m is used for comparison study. In the present study, all geometrical lengths are normalized with the mean diameter D_m.

3. Numerical method

In the present study, unsteady three-dimensional laminar flow of a viscous incompressible fluid is considered. The finite volume method (FVM) with an unstructured hexahedral grid is employed to solve the unsteady three-dimensional incompressible Navier–Stokes equations.

3.1. *Governing equations*

The three-dimensional dimensionless Navier–Stokes equations governing the flow of a Newtonian fluid can be written in vector form as

$$\frac{\partial \boldsymbol{u}}{\partial t} + \boldsymbol{u} \cdot \nabla \boldsymbol{u} = -\nabla p + \frac{1}{Re}\nabla^2\boldsymbol{u}, \tag{3.1}$$

$$\nabla \cdot \boldsymbol{u} = 0, \tag{3.2}$$

where $\boldsymbol{u}$ is the non-dimensional flow velocity vector in the Cartesian coordinate system (x, y, z) with its three velocity components u, v and w. The non-dimensional static pressure is denoted by p. $Re = U_\infty D_m/\nu$ is the Reynolds number, with U_∞ being the free-stream velocity and ν being the fluid kinematic viscosity. In solving the governing equations, the different physical quantities are changed to non-dimensional form; i.e. all the variables are normalized. The flow time t is normalized by the free-stream velocity and the cylinder mean diameter, such that $\tilde{t} = tU_\infty/D_m$. In the above equations the velocities are non-dimensionalized by the free-stream velocity U_∞.

The present FVM code calculates the solution of the incompressible Navier–Stokes equations. The spatial discretization of the equations is based on an unstructured hexahedral mesh. The primitive variables are all discretized in a cell-centred fashion, with one value for each variable in each element. The semi-implicit pressure linked equations (SIMPLE) method is used to deal with the pressure velocity coupling between the momentum and the continuity equations. The second-order upwind differencing scheme is used for convective terms. Second-order central differencing scheme is adopted for diffusion terms, while the second-order implicit scheme is employed to advance the equations with time.

3.2. *Computational domain and boundary conditions*

In the present study, the computational domain used for the simulations is set at $24D_m \times 36D_m \times \lambda$ in x, y, z directions of a fixed Cartesian coordinate system (x, y, z), respectively as shown in figure 15 in the appendix. The domain parameters are similar to that chosen by Darekar & Sherwin (2001*a*, *b*). A wavy cylinder model is placed inside the flow domain. The x-axis is chosen to be along the inlet main flow direction (streamwise direction); the z-axis is parallel to the cylinder axis (spanwise direction); and the y-axis is perpendicular to both x-axis and z-axis (crosswise direction). The origin $(0, 0, 0)$ of the coordinate is set at the centre of the nodal cross-section of the wavy cylinder. The velocity at upstream boundary of the computational domain is set at a distance of $12D_m$ from the centreline of the cylinder, while the downstream boundary is $24D_m$ away from the wavy cylinder. Each lateral surface is $12D_m$ away from the axis of the cylinder (blockage $\approx 4.2\,\%$). Furthermore, for the computational domain along the spanwise direction, only one wavelength λ is adopted due to periodic boundary condition being used in the simulation.

The boundary conditions are summarized in the following manner: At the inlet boundary, a uniform velocity profile $(u = 1, v = w = 0)$ is imposed. A convective boundary condition $(\partial \boldsymbol{u}/\partial t + U_c(\partial \boldsymbol{u}/\partial x) = 0)$ is used at the outlet boundary, where U_c is the characteristic convective velocity (surface-averaged streamwise velocity) at the plane of the outlet. A periodic boundary condition is employed at the boundaries in the spanwise direction, and no-slip boundary condition $(u = v = w = 0)$ is prescribed at the surface of the wavy cylinders. The lateral surfaces are treated as slip surfaces, using symmetry boundary conditions $(\partial u/\partial y = \partial w/\partial y = v = 0)$. The accuracy of computational results is highly dependent on the grid size and number of cells. Details of the grid independence tests and the validation of the numerical models are provided in the Appendix.

3.3. *Definition of dimensionless physical quantities*

The important dimensionless physical quantities are summarized below. In the present calculations, the drag coefficient C_D and lift coefficient C_L are defined by

$$C_D = \frac{2F_D}{\rho U_\infty^2 D_m \lambda}, \tag{3.3}$$

$$C_L = \frac{2F_L}{\rho U_\infty^2 D_m \lambda}, \tag{3.4}$$

where ρ is the fluid density; F_D and F_L are the total drag force and total lift force, respectively; $\bar{C}_D$ is the mean drag coefficient; and C_L' is the r.m.s. lift coefficient. The Strouhal number is the non-dimensional vortex shedding frequency f_s and is expressed as

$$St = \frac{f_s D_m}{U_\infty}. \tag{3.5}$$

The frequency of vortex shedding f_s is obtained by fast Fourier transform (FFT) of the lift fluctuating-time history. The pressure coefficient C_P on the cylinder surface is defined as

$$C_p = \frac{2(P - P_\infty)}{\rho U_\infty^2}, \tag{3.6}$$

where P_∞ is the oncoming flow static pressure, and P is the static pressure on the cylinder surface. The mean base pressure coefficient $-\bar{C}_{pb}$ is the value of negative

non-dimensional mean pressure at the rear stagnation point (180° from the frontal point) of the cylinder.

The definition of the velocity recovery length (vortex formation length L_f) by Lam *et al.* (2004*b*) is adopted in the present study. The location of the closure point ($U/U_\infty = 0$) of the time-averaged streamwise velocity U on the wake centerline ($y = 0$ plane) has been used to define the vortex formation length L_f. The flow separation point in the boundary layer is determined at the position on the cylinder wall at which the shear stress is zero. The separation angle is the angle measured from the frontal stagnation point to the separation point.

4. Results and discussions

The present study focuses attention on investigating the characteristics of flow past wavy cylinders at low Reynolds numbers. A series of computational investigations have been carried out mainly at Reynolds number equal to 100 for wavy cylinders with wavelength ratio $\lambda/D_m = 1$ to 10 and wave amplitude ratio $a/D_m = 0.02$ to 0.30. Comparisons are made with a straight circular cylinder ($\lambda/D_m = \infty$, $a/D_m = 0$). The three-dimensional vortex structures are captured and classified. Other physical parameters such as velocity, pressure, drag, lift and vortex formation length are obtained to provide better understanding of the phenomena.

4.1. *Force distributions* ($1 \leqslant \lambda/D_m \leqslant 10$, $0.05 \leqslant a/D_m \leqslant 0.25$, $Re = 100$)

Figure 4 summarizes the variations of the mean drag coefficient $\bar{C}_D$ and the r.m.s. lift coefficient C'_L with different wave amplitude ratios and wavelength ratios of the wavy cylinders. The values of $\bar{C}_D$ and C'_L of a corresponding straight circular cylinder with diameter equal to the mean diameter (D_m) are also incorporated for comparison. The value of $\bar{C}_D$ and C'_L of a straight circular cylinder at $Re = 100$ for the present simulation are 1.34 and 0.234, respectively. In figure 4, two troughs are found for both the mean drag coefficient curve and the r.m.s. lift coefficient curve at positions around $\lambda/D_m = 2.5$ and $\lambda/D_m = 6$ for wave amplitude $a/D_m > 0.1$. The drop at the second trough at $\lambda/D_m = 6$ is severer than that at the first trough with a maximum drag reduction of about 18 % and the r.m.s. lift approaching zero. For a constant a/D_m and an increased λ/D_m, the values of $\bar{C}_D$ and C'_L reduce quickly when $\lambda/D_m \leqslant 2$ but increase to a maximum again at $\lambda/D_m = 3$. Compared with a circular cylinder, the mean drag coefficient and the r.m.s. lift coefficient start to drop below the values of a circular cylinder at the positions $\lambda/D_m = 1.75$ and 1.25, respectively. At this lower range of wavelength ratio ($1 \leqslant \lambda/D_m \leqslant 3$), although the maximum drag coefficient reduction is only up to 9 %, the maximum r.m.s. lift coefficient is reduced to 0.0164 which is much smaller than the reduction of a circular cylinder. The values of $\bar{C}_D$ and C'_L begin to rise at $\lambda/D_m = 2.5$ to until they reach the maximum at $\lambda/D_m = 3$. It can be seen that around $\lambda/D_m = 3$, no drag reduction is obtained for the wavy cylinder, while there are still slight reduction in r.m.s. lift coefficient for large amplitude ratio a/D_m. Further increasing the wavelength, the values of $\bar{C}_D$ and C'_L drop again to very low values at $\lambda/D_m = 5$. The minimum values of $\bar{C}_D$ and C'_L are found at $\lambda/D_m = 6$ (the value of the second trough point). After that, $\bar{C}_D$ and C'_L start to increase again moderately with the wavelength for $\lambda/D_m \geqslant 6$. The maximum drag coefficient reduction of up to 18 % is found for the wavy cylinder at the values $\lambda/D_m = 6$ and $a/D_m = 0.25$ (see figure 4*a*), while the r.m.s. lift coefficient is equal to zero at $\lambda/D_m = 6$ and $a/D_m = 0.15$. The zero r.m.s. lift implies that there is no vortex shedding at the near wake of such wavy cylinders. Considering the previous experimental and numerical results by Lam *et al.* (2004*a*), Lee & Nguyen (2007) and
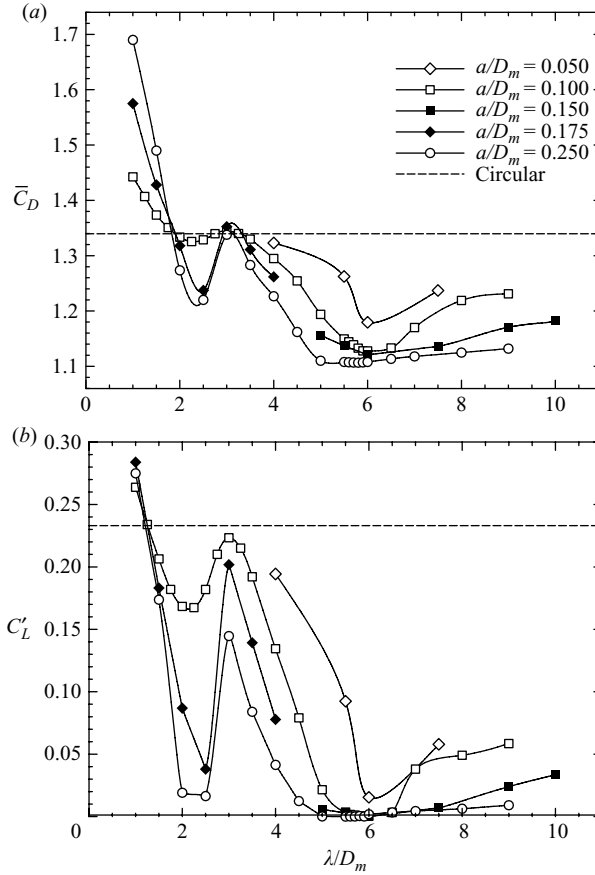
FIGURE 4. Mean drag coefficients $\bar{C}_D$ and r.m.s. lift coefficients C'_L for wavy and circular cylinders at $Re = 100$ with different wavelengths λ/D_m and wave amplitudes a/D_m.

Lam & Lin (2008), the optimal wavelength λ/D_m of the present results in the lower range of wavelength ratio ($1 \leqslant \lambda/D_m \leqslant 3$, $Re = 100$) appears to be in the range 2–2.5, which is slightly higher than that for turbulent flow at high Reynolds number (around 1.9). In previous investigations for both laminar and turbulent flows, all the curves of $\bar{C}_D$ and C'_L for different λ/D_m with constant a/D_m show a 'trough' characteristic, since the results have only been obtained over a small range of wavelength around the first trough. It can be seen from the present simulations in a broader range of wavelength ratio ($1 \leqslant \lambda/D_m \leqslant 10$) that there is a first 'trough' followed by a bigger second 'trough'. At least for $Re = 100$, the true optimal wavelength appears to be close to $\lambda/D_m = 6$. This result is similar to that found by Darekar & Sherwin (2001b) for a square circular with wavy stage face. The optimal wavelength found by them is 5.7 at $Re = 100$ with a drag reduction up to 16 %. It is also close to that of the circular cylinder, found using active control method (Kim & Choi 2005). The mean drag coefficient was reduced about 20 % with the optimal wavelength between 4 and 5 at $Re = 100$.

Furthermore, a larger value of a/D_m will give a more significant reduction of drag and suppression of r.m.s. lift. With a large value of wave amplitude a, the mean drag coefficients of wavy cylinders are significantly reduced for the same λ/D_m when λ/D_m is larger than 1.75, while the r.m.s. lift coefficients are also drastically reduced when
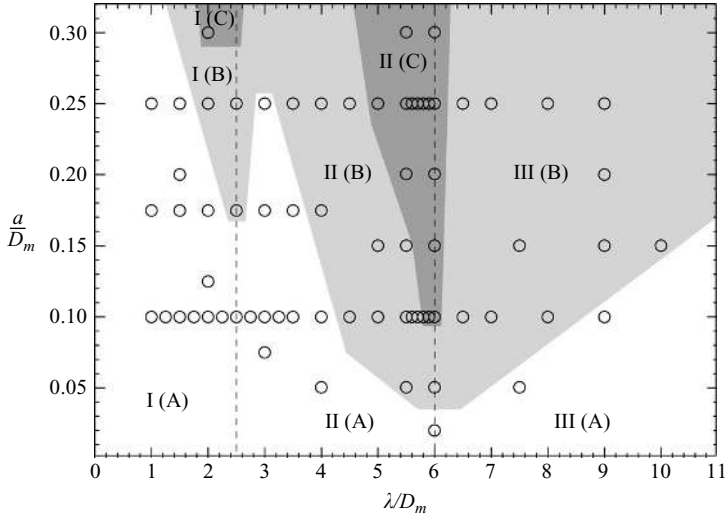
FIGURE 5. Flow pattern regimes of wavy cylinders with different spanwise wavelengths λ/D_m and wave amplitudes a/D_m at $Re = 100$. The symbol $\circ$ represents each wavy cylinder case in the present simulations.

λ/D_m is larger than 1.25. However, with the values $\lambda/D_m \leqslant 1.75$ for drag coefficient and $\lambda/D_m \leqslant 1.25$ for r.m.s. lift coefficient, a large value of a/D_m, on the contrary, leads to an increase of $\bar{C}_D$ and C'_L in such Reynolds number range.

4.2. *Flow pattern regimes* $(1 \leqslant \lambda/D_m \leqslant 10, 0.05 \leqslant a/D_m \leqslant 0.25, Re = 100)$

To understand the variations in drag and r.m.s. lift and the occurrence of the first trough and the second trough, the flow patterns for different wavy cylinders are captured. The wavy cylinders over the whole range of wavelength and wave amplitude investigated and classified into three wavelength regimes (I, II and III) with three different flow patterns (A), (B) and (C) as shown in figure 5. The spanwise vorticity $\omega_z = \partial v/\partial x - \partial u/\partial y$ at different spanwise sections was used as a flow indicator. The three-dimensional vortex structures corresponding to different flow patterns are shown in figure 6. The time histories of some typical wavy cylinders are also incorporated for comparison of flow patterns and force characteristics. Flow pattern (A) is similar to the wake structure behind a straight circular cylinder except with some distortions in the spanwise direction. Flow pattern (B) is characterized by an increase of three-dimensional wake vortex distortion and increase of vortex formation length with a progressive weakening of vortex shedding, while for flow pattern (C), the free shear layer does not roll up into a vortex, and hence no vortex shedding occurs.

The flow pattern regimes I, II and III correspond to different wavelength regimes in the range of $1 \leqslant \lambda/D_m \leqslant 2.5$, $2.5 \leqslant \lambda/D_m \leqslant 6$ and $6 \leqslant \lambda/D_m \leqslant 10$, respectively. It is to be noted that the division lines are drawn at the positions of maximum reduction in drag and r.m.s. lift at $\lambda/D_m = 2.5$ and 6, so that the change of flow patterns around these positions can be clearly illustrated. It can be seen from figure 6 that the reduction of drag and r.m.s. lift in the three regimes is due to the transformation of flow pattern from pattern (A) to pattern (B) and then to pattern (C) in the three regimes. The prominent features for the wavy cylinders in different flow pattern regimes are summarized in table 2. The flow structures in the nodal plane are not identical with those in the saddle plane due to the three-dimensional effect. In regime I $(1 \leqslant \lambda/D_m < 2.5)$ and regime II $(2.5 \leqslant \lambda/D_m < 4)$, the vortices expand along both the
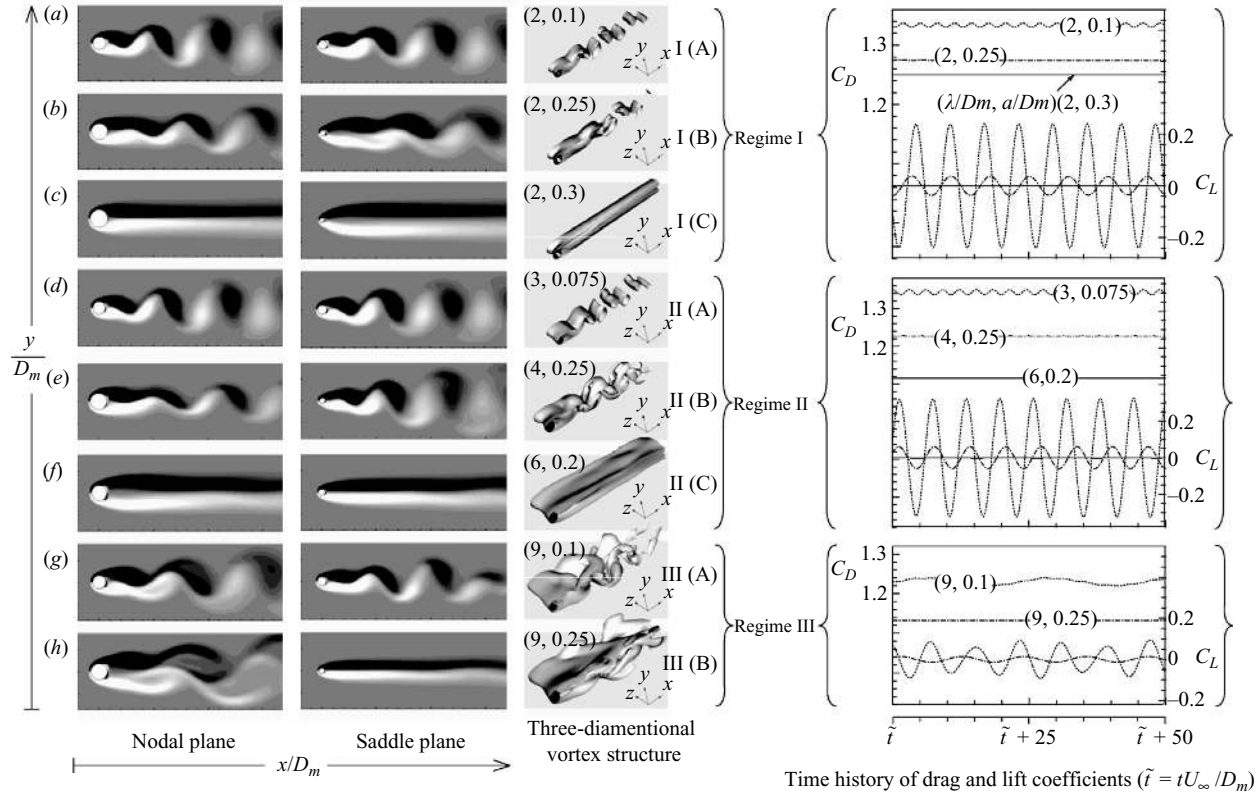
FIGURE 6. Flow patterns for different wavy cylinders at $Re = 100$: λ/D_m and a/D_m are respectively denoted by the values in parentheses.

Flow mode		Key features	
		Near wake flow structures	Force reduction
Regime I $1 \leqslant \lambda/D_m \leqslant 2.5$, $0.1 \leqslant a/D_m \leqslant 0.3$	I (A)	Quasi-two-dimensional wake, similar to that of a straight circular cylinder; slight spanwise distortions.	No drag reduction, r.m.s. lift is evident; $St_{(WY)} \approx St_{(CY)}$
	I (B)	Noticeable free shear layer elongation towards the downstream direction.	Drag reduction with the weakening of r.m.s. lift; $St_{(WY)} \leqslant St_{(CY)}$
	I (C)	Steady and symmetrical wake; first disappearance of periodic vortex shedding phenomenon.	Significant drag reduction and full suppression in r.m.s. lift; $St_{(WY)} = 0$; first optimal wavelength ratio.
Regime I↔II (small optimal wavelength $\lambda/D_m = 2.5$)			
Regime II $2.5 \leqslant \lambda/D_m \leqslant 6$, $0.02 \leqslant a/D_m \leqslant 0.3$	II (A)	Similar to that of in regime I (A); more spanwise distortions.	Drag and lift are close to or slightly smaller than those of circular cylinders; $St_{(WY)} \leqslant St_{(CY)}$
	II (B)	Fully three-dimensional wake; evident spanwise distortions; the strength of vortices is weakening.	Evident drag reduction and suppression in r.m.s. lift; $St_{(WY)} < St_{(CY)}$
	II (C)	Well controlled, steady and symmetrical wake patterns; no vortex shedding occurs.	Maximum drag reduction and no r.m.s. lift; $St_{(WY)} = 0$; Real optimal wavelength ratio.
Regime II↔III (large optimal wavelength $\lambda/D_m = 6$)			
Regime III $6 \leqslant \lambda/D_m \leqslant 10$, $0.05 \leqslant a/D_m \leqslant 0.25$	III (A)	Prominent complicated three-dimensional wake; vortex dislocation appears with the weakening of vortices strength.	Drag reduction and the weakening of r.m.s. lift; $St_{(WY)} \leqslant St_{(CY)}$
	III (B)	Fully complicated three-dimensional wake; spanwise direction expansion of the regime II (B) wake patterns.	Evident drag reduction and suppression in r.m.s. lift; $St_{(WY)} < St_{(CY)}$

TABLE 2. Summary of flow patterns of different wavy cylinders at $Re = 100$: WY = wavy cylinder; CY = circular cylinder.

streamwise direction and the crosswise direction. The wake width in the saddle plane is increased, giving rise to a wide wake further downstream (figure 6*a–b*, *d–e*). On the contrary, the vortices in the nodal plane appear to be elongated in the streamwise direction and noticeably compressed in the crosswise direction. The flow separation occurs later at the nodal position than that at the saddle position. As a result, it produces a narrower wake downstream in the nodal plane. In such smaller wavelength regime, similar characteristic of flow pattern (B) was found by Ahmed *et al.* (1993) for a wavy cylinder with $\lambda/D_m = 1.2$ and $a/D_m = 0.1$ at Re from 5000 to 20 000. Lam *et al.* (2004*b*) showed similar flow characteristics of pattern (A) at $Re \leqslant 400$ and pattern (B) at $Re \geqslant 600$ for a wavy cylinder with $\lambda/D_m = 2.27$ and $a/D_m = 0.09$. Lam & Lin (2008) also found the flow pattern (B) with $1.14 \leqslant \lambda/D_m \leqslant 3.33$ and $0.09 \leqslant a/D_m \leqslant 0.15$.

In regime II with $4 < \lambda/D_m \leqslant 6$ and regime III, the wake pattern in the nodal plane is wider than that in the saddle plane (see figure 6*f–h*). It is opposite the regimes discussed above. Due to the effect of vortex dislocation along the spanwise direction, the drag coefficient C_D varies in a larger time scale cycle ($\lambda/D_m = 9$ and $a/D_m = 0.1$, in regime III (A); see figure 6*g*). It is evidently different from other wavy cylinders in regimes I and II. Similar results were observed by Darekar & Sherwin (2001*b*; $\lambda/D_m = 10$, wavy square cylinder) and Kim & Choi (2005; $\lambda/D_m = 7$, circular cylinder by active control method) at the similar Reynolds number $Re = 100$. With the increase of a/D_m, such phenomenon disappears. For constant values of λ/D_m, a large value of a/D_m means a steeper wavy surface along the spanwise direction. A steeper wavy surface will then give rise to different angle of flow separation along the spanwise direction. In the nodal plane, the far downstream wake width is much different from that in the saddle plane. It makes a large degree of distortion of the near wake structures formed in regime II (B) and regimes III (A) and III (B). It is interesting to note that no periodic vortex shedding appears in the saddle plane in regime III (B) (see figure 6*h*). The wake of the saddle plane shows a steady plane vortex sheet similar to the saddle plane flow pattern in regime II (C).

For pattern (C), the flow behind the wavy cylinder is close to a steady plane vortex sheet. The force reduces sharply with the r.m.s. lift of the wavy cylinder being greatly suppressed. In general, only weak vortex shedding can be found at the very far downstream positions. For the optimal wavy cylinder models ($\lambda/D_m = 2$, $a/D_m = 0.3$ and $\lambda/D_m = 6$, $a/D_m = 0.15$), the periodic vortex shedding cannot be discerned. The symmetrical and steady plane vortex sheets do not roll up into vortex structures. The value of Strouhal number becomes zero. These characteristics are also reflected by the distributions of different time histories of drag and lift coefficients (see figure 6). As the value of a/D_m, in regime II increases, the value of C'_L becomes discernible again ($C'_L = 0.0006$), and slight vortex shedding appears very far downstream with $St = 0.091$ for a wavy cylinder for $\lambda/D_m = 6$ and $a/D_m = 0.2$ (see figure 6*f*).

To understand why free shear layer will not roll up into a vortex easily at optimal wavelength, the spanwise variation of vorticity in the shear layers which leads to additional vorticity components in the streamwise direction is studied. Figure 7 shows the streamwise vorticity isosurface for flow around the optimal wavy cylinder ($\lambda/D_m = 6$ and $a/D_m = 0.15$). Two types of stable streamwise vorticities can be observed – an outer streamwise vorticity and an inner streamwise vorticity. The central position of the outer streamwise vorticity is closer to the surface of the wavy cylinder than that of the inner one. Both the outer and inner streamwise vorticities are well organized and exhibit symmetrical distributions of vorticity in the *x–z* plane with $y = 0$, while at the same time showing a periodic repetition along the spanwise
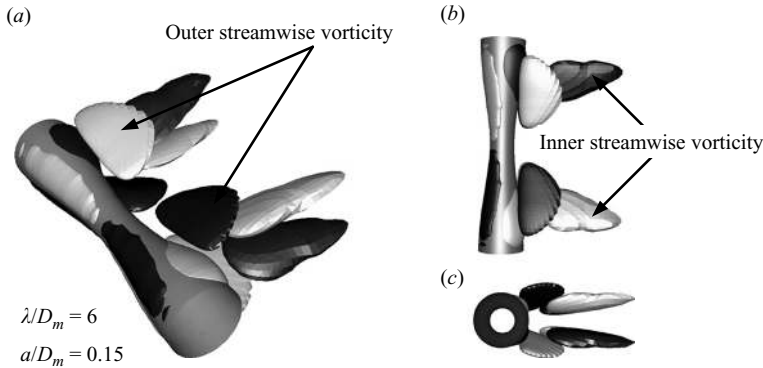
FIGURE 7. Streamwise vorticity isosurface plot for the flow around a wavy cylinder at optimal wavelength for $Re = 100$: (a) overview; (b) the same structures viewed in the x–z plane and (c) the x–y plane.
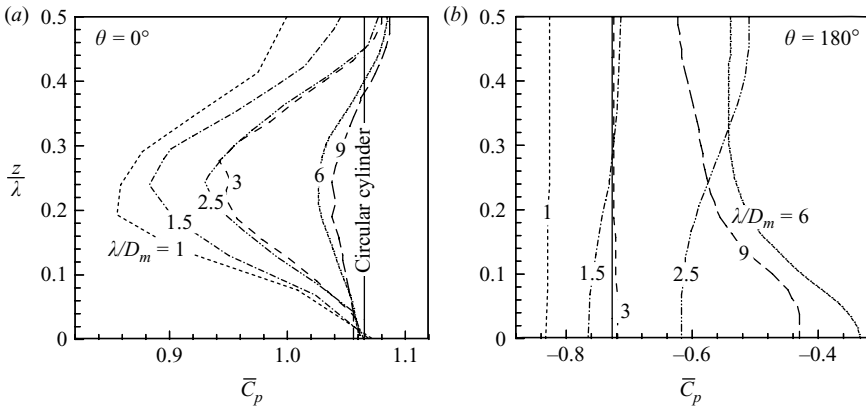

FIGURE 8. Spanwise distributions of the mean pressure coefficients for different wavy cylinders at $Re = 100$: (a), (b) $a/D_m = 0.175$; (c) (d) $a/D_m = 0.15$. The position of $z/\lambda = 0$ denotes the node point, while $z/\lambda = 0.5$ is the saddle point.

direction. This kind of additional streamwise component tends to stabilize the two-dimensional spanwise vorticity of the free shear layers. The free shear layers separated from the surface of the wavy cylinder are pushed to further downstream positions as shown in figure 6 (patterns B and C). This stable three-dimensional redistribution of vorticity appears to prevent the free shear layer interaction in the near wake behind the cylinder and hence suppresses the formation of Kármán vortex.

4.3. Flow characteristics of typical wavy cylinders at $Re = 100$

To deepen our understanding of the effects of change of wavelength and wave amplitude, the surface pressure distribution, the vortex formation length, the surface velocity separation angles and the three-dimensional vortex structures of some typical wavy cylinders are obtained and investigated.

4.3.1. Base pressure coefficient and vortex formation length

Figure 8 shows the spanwise direction mean pressure coefficient $\bar{C}_p$ distributions of several wavy cylinders at the positions of $\theta = 0°$ and $180°$. At the position $\theta = 0°$, the values of $\bar{C}_p$ are generally smaller than those for a circular cylinder along the spanwise direction at $Re = 100$, except at the positions of nodal and saddle planes (see
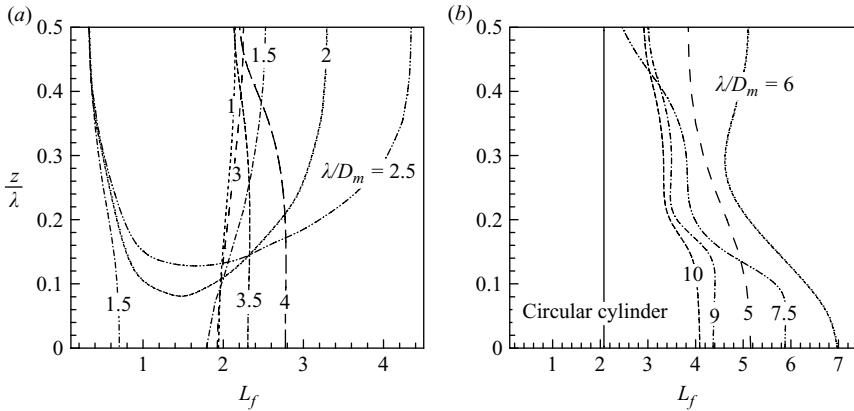
FIGURE 9. Spanwise distributions of the vortex formation length (L_f) for different wavy cylinders at $y = 0$ with the mean steamwise velocity equal to zero ($Re = 100$): (a) $a/D_m = 0.175$; (b) $a/D_m = 0.15$. The position of $z/\lambda = 0$ denoted the node, while $z/\lambda = 0.5$ is saddle point.

figure 8a). At the middle section ($z/\lambda = 0.25$), the mean pressure coefficients at $\theta = 0°$ of all the wavy cylinders are smaller than those in other planes of the wavy cylinders. The value of $\bar{C}_p$ decreases with the decrease in λ/D_m for the same wave amplitude ($a/D_m = 0.175$, $1 \leqslant \lambda/D_m \leqslant 3$ and $a/D_m = 0.15$, $\lambda/D_m = 6$ and 9). This means larger wave steepness a/λ can increase the variation of the spanwise pressure coefficients and also that it gives rise to a strong three-dimensional effect on the near wake of wavy cylinders. Similar results were also obtained by Ahmed & Bays-Muchmore (1992), Lam *et al.* (2004a) and Lam & Lin (2008) with $\lambda/D_m \leqslant 2.27$ for turbulent flow.

Figure 8(b) shows the mean pressure coefficients $\bar{C}_p$ of different wavy and circular cylinders at the rear position $\theta = 180°$. In general, the maximum value of $\bar{C}_p$ (the minimum value of base pressure coefficient $-\bar{C}_{pb}$) along the spanwise direction is obtained at $\lambda/D_m = 2.5$ ($1 \leqslant \lambda/D_m \leqslant 3$, $a/D_m = 0.175$), while the value of $\bar{C}_p$ shows little variation along the spanwise direction for wavelength $\lambda/D_m = 1$, and it is smaller than that of a circular cylinder. A stronger base suction leads to a higher drag (figure 4a). Increase in the wavelength ($1 \leqslant \lambda/D_m \leqslant 2.5$) leads to increase in the value of $\bar{C}_p$ from the nodal position ($z/\lambda = 0$) to the saddle position ($z/\lambda = 0.5$). Similar results were also obtained by Ahmed & Bays-Muchmore (1992), Lam *et al.* (2004a) and Lam & Lin (2008) with $\lambda/D_m \leqslant 2.27$ for turbulent flow. When $\lambda/D_m = 3$, the value of $\bar{C}_p$ is close to that of a circular cylinder. As the value of the wavelength further increases, however, the value of $\bar{C}_p$ decreases from the nodal position to the saddle position. The maximum $\bar{C}_p$ is obtained at $\lambda/D_m = 6$. It means that the minimum value of $-\bar{C}_{pb}$ corresponds to the maximum drag reduction. Apart from the wavy cylinders with $\lambda/D_m = 1$, 1.5 and 3, all the value of $\bar{C}_p$ along the spanwise direction are larger than that of a corresponding circular cylinder.

The length of the reversed flow region behind the bluff bodies has a strong relationship with the mean base pressure coefficient $-\bar{C}_{pb}$. Lam *et al.* (2004b) and Lam & Lin (2008) showed that the values of the velocity recovery lengths of both wavy and circular cylinders are inversely proportional to the values of the mean base pressure coefficient $-\bar{C}_{pb}$ in turbulent flow. Similar trend can be found in laminar flow condition. Figure 9 shows that the general trend of spanwise distribution of vortex formation length is similar to the spanwise distribution of the mean pressure coefficient $\bar{C}_p$ at $\theta = 180°$ (see figure 8) for all the wavy cylinders. Along the spanwise direction of wavy cylinders, the values of L_f exhibit a large variation. For the typical
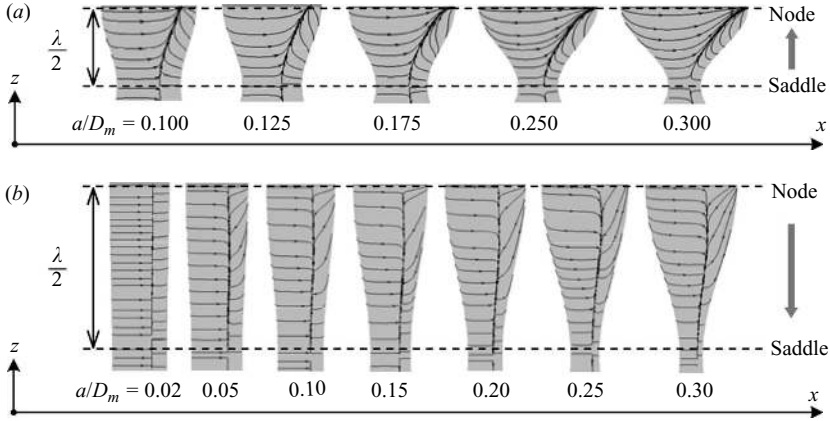
FIGURE 10. Mean surface streamlines of wavy cylinders with different wave amplitude at $Re = 100$: (a) $\lambda/D_m = 2$; (b) $\lambda/D_m = 6$.

wavy cylinder with $\lambda/D_m = 1.5$ and $a/D_m = 0.175$, the value of L_f shows in two line distributions along the spanwise direction due to the definition adopted (see figure 9a). The line close to the back surface ($\theta = 180°$) of the wavy cylinder is not the real vortex formation length. The second line is the real vortex formation length, considering the relationship between L_f and $-\bar{C}_{pb}$. Furthermore, we also found that at the nodal position and the mean values of streamwise velocity U/U_∞ in the $y = 0$ plane are not equal to zero for the wavy cylinders with $\lambda/D_m = 2$ and 2.5. Along the spanwise direction, the value $U/U_\infty = 0$ can be captured at $z/\lambda \geqslant 0.08$ for $\lambda/D_m = 2$ and at $z/\lambda \geqslant 0.13$ for $\lambda/D_m = 2.5$. The central position of the streamwise velocity recovery appears around the saddle position of the wavy cylinder. However, it is far from the back surface of the wavy cylinder and leads to a small value of $-\bar{C}_{pb}$. In figure 9(b), the values of the vortex formation length L_f of all wavy cylinders are evidently longer than that of a circular cylinder. At the nodal positions, the vortex formation lengths are longer than that in the saddle plane in the range $3.5 \leqslant \lambda/D_m \leqslant 10$. In general, the vortex formation length increases from the nodal plane to the saddle plane. Unlike that of the wavy cylinders with $1.5 \leqslant \lambda/D_m \leqslant 2.5$, the streamwise velocity recovery centre moves to the nodal sections. An evidently different vortex structure is generated along the spanwise direction. The wake pattern in the nodal plane is much wider than that in the saddle plane (figure 5g, h). Despite the difference of wake structures, velocity and pressure distributions, it can be concluded that longer vortex formation region can provide more reduction of the drag coefficient and a much greater suppression of the r.m.s. lift coefficient.

4.3.2. *Velocity separation angles*

Figure 10 shows the time-averaged surface streamlines with the variation of wave amplitude $0.1 \leqslant a/D_m \leqslant 0.3$ ($\lambda/D_m = 2$) and $0.02 \leqslant a/D_m \leqslant 0.3$ ($\lambda/D_m = 6$) at $Re = 100$. The velocity separation lines are also drawn along the spanwise direction. In general, the separation position varies from the nodal plane to the saddle plane. Lam *et al.* (2004b) pointed out the significant spanwise flow motion from the saddle plane towards the nodal plane when $\lambda/D_m = 2.27$ for Re between 3000 and 9000, while Lam & Lin (2008) also found such phenomenon for turbulent flow with $1.14 \leqslant \lambda/D_m \leqslant 3.33$ at $Re = 3000$. Similar phenomenon is observed in laminar flow condition with $\lambda/D_m = 2$ and $0.1 \leqslant a/D_m \leqslant 0.3$ (see figure 10a). As shown in figure 11(a), the mean
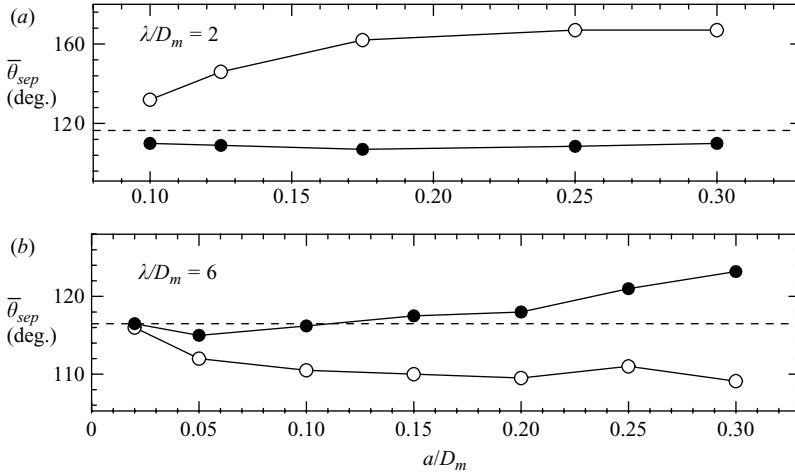
FIGURE 11. Mean velocity separation angles of wavy cylinders with different wave amplitude at $Re = 100$: (a) $\lambda/D_m = 2$; (b) $\lambda/D_m = 6$. ----, circular cylinder; —○—, nodal plane; —●—, saddle plane.

velocity separation angle $\bar{\theta}_{sep}$ in the nodal plane is larger than that in the saddle plane $\lambda/D_m = 2$. It means that flow separation occurs earlier at the saddle position and later at the nodal position and hence gives rise to the distortion of free shear layer and the formation of three-dimensional vortex structures. It also leads to the flow motion from the saddle plane to the nodal plane and the generation of a sinusoidal wave line along the spanwise direction. The wavy velocity separation line becomes progressively clear with the increase in a/D_m. It means that the wave steepness value a/λ plays an important role in the determination of the separation point. The stability of the free shear layer and the resulting vortex structure are highly dependent on the separation point of the wavy cylinder. For a wavy cylinder with a larger value of wavelength ($\lambda/D_m = 6$; see figure 10b), the separation line shows little waviness with the small value $a/D_m = 0.02$. With the increase in a/D_m, the variation becomes clearer. All the values of $\bar{\theta}_{sep}$ in the nodal planes are less than those in the saddle planes (see figure 11b). It means that flow separation at the nodal position is much earlier than that at the saddle position for all wavy cylinders with $\lambda/D_m = 6$. The spanwise flow motion moves from the nodal plane towards the saddle plane, opposite to those shown in figure 10(a) with $\lambda/D_m = 2$. At $a/D_m < 1.5$ the values of the separation angle in both the nodal and saddle planes are less than that of circular cylinder, while at the saddle plane, it is larger than that of the circular cylinder when $a/D_m > 1.5$. Similar results were also obtained using an active control method at the same Reynolds number with $\lambda/D_m = 5$ by Kim & Choi (2005). Because of the wavy velocity separation line, the two-dimensional vortex sheet is distorted, and the vortex structures become highly three-dimensional in the wake of the wavy cylinder. That means a longitudinal vorticity component is produced resulting from the wavy separation line. Thereafter, the three-dimensional vortex sheet rolls up into complex three-dimensional vortex structure at further downstream positions.

4.3.3. *Spanwise wake structure topology*

Figure 12 shows the spanwise vortex structure distributions for several typical wavy cylinders. The wake structures are plotted with several periodic repetitions along the spanwise direction. With a small value of spanwise wavelength, the
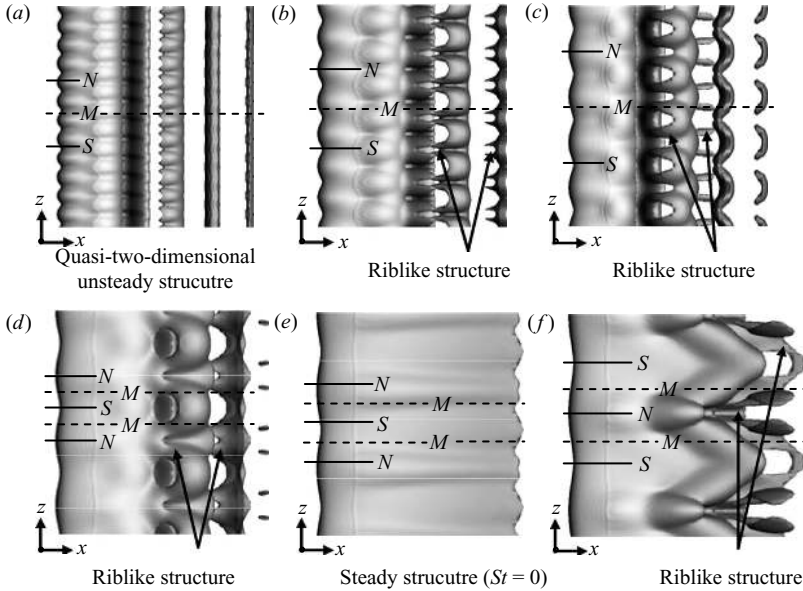
FIGURE 12. The instantaneous spanwise vortex structure distributions with several periodic repetitions along the spanwise direction ($Re = 100$): (a) $\lambda/D_m = 1.5$ and $a/D_m = 0.175$; (b) $\lambda/D_m = 2.5$ and $a/D_m = 0.175$; (c) $\lambda/D_m = 3.5$ and $a/D_m = 0.175$; (d) $\lambda/D_m = 5$ and $a/D_m = 0.15$; (e) $\lambda/D_m = 6$ and $a/D_m = 0.15$; (f) $\lambda/D_m = 7.5$ and $a/D_m = 0.15$. The symbols N, M and S denote the nodal, middle and saddle planes, respectively.

three-dimensional feature is not prominent at the further downstream positions (see figure 12a, $\lambda/D_m = 1.5$ and $a/D_m = 0.175$, in the flow pattern (A) in regime I). The wake pattern is close to that of a circular cylinder at $Re = 100$ (two-dimensional unsteady wake vortex shedding flow pattern). With $\lambda/D_m = 2.5$, the three-dimensional vortex structures become clearer. The riblike vortex structures captured are similar to the spanwise vortex structures of the wavy cylinder ($\lambda/D_m = 2.27$ and $a/D_m = 0.09$) at $Re = 600$ obtained by the laser-induced fluorescence (LIF) method (Lam *et al.* 2004b). Furthermore, the riblike vortex structure in the near wake of the wavy cylinder appears at the positions of saddle planes (see figure 12b, regime I↔II (B)). It also shows a periodic characteristic along the spanwise direction. As shown in figure 12(c, d) in regimes II (A, B), as the values of λ/D_m further increased from 3.5 to 5.0, the three-dimensional feature became more and more prominent. The riblike vortex structures along the spanwise direction were also observed. However, they appear at the positions near the nodal plane, different from that in figure 12(b). Considering the flow separation characteristics for wavy cylinders with different wavelength (figures 10 and 11), the riblike vortex structures appear at the positions at which the separation of the flow occurs first. The free shear layers behind the wavy cylinder at such positions expand along both the streamwise direction and the crosswise direction while shrink at other positions. It distorts the spanwise wake structures, and the evidently three-dimensional wake structures are thus generated. With a larger waviness of the wavy cylinder, the riblike structures become more prominent. As discussed in §4.3.2, there is a significant spanwise flow motion from the saddle plane towards the nodal plane for smaller wavelength ($\lambda/D_m = 2$), while the flow motion is from the nodal plane to the saddle plane for larger wavelength ($\lambda/D_m = 6$). It implies that the different spanwise flow motion with the variation of wavelength may lead to

different additional vorticity components which hence give rise to two types of riblike structures (at the saddle or nodal position) being generated as shown in figure 12.

For the optimal spanwise wavelength $\lambda/D_m = 6$ corresponding to the flow pattern regime II (C), the spanwise vortex structures appear as a smooth plane vortex sheet along the spanwise direction from the nodal position to the saddle position. The riblike structures disappear (see figure 12e). Only two wide and smooth vortex sheets are generated behind the wavy cylinder (the flow pattern in figure 6f). Unlike a two-dimensional vortex sheet, the three-dimensional vortex sheet behind the optimal wavy cylinder is very stable and will not roll up into a mature vortex at this Reynolds number even at very far downstream position. The periodic vortex shedding is well suppressed at $\lambda/D_m = 6$ and $a/D_m = 0.15$. Therefore, the largest reduction of the mean drag coefficient and the r.m.s. lift coefficient is obtained. At $\lambda/D_m = 7.5$ and $a/D_m = 0.15$, the riblike structures appear again (figure 12f) at the positions of nodal planes, while structures are very different from that of figure 12(b–d) for such large value of spanwise wavelength. The flow pattern characteristic in regime III (B) is fully demonstrated.

4.4. *Reynolds number effect*

Reynolds number plays an important role in the effect of optimal spanwise wavelength in controlling the vortex shedding, drag reduction and suppression of the vortex-induced vibrations. Several typical wavy cylinders are used to examine the effects of Reynolds numbers from 60 to 150. A corresponding circular cylinder is also simulated at the same Reynolds numbers for comparison. The mean drag coefficient $\bar{C}_D$, the r.m.s. lift coefficient C'_L and the Strouhal number St for the wavy and circular cylinders at different Reynolds numbers are obtained.

Figure 13(a–c) shows that the maximum drag reduction of up to 21.5 % is obtained at $Re = 150$ with $\lambda/D_m = 2.5$ with the r.m.s. lift coefficient $C'_L = 0$ and the Strouhal number $St = 0$ in the range $1.5 \leqslant \lambda/D_m \leqslant 3.0$ and $a/D_m = 0.175$. In this spanwise wavelength range at $Re = 60$, the minimum value of $\bar{C}_D = 1.426$ is obtained for $\lambda/D_m = 3$ and is close to the value of a circular cylinder at the same Reynolds number ($\bar{C}_D = 1.428$). The value of $\bar{C}_D$ decreases as the value of λ/D_m increases. The lift fluctuation is not significantly weakened with little change of the Strouhal number. At $Re = 80$, the minimum value of $\bar{C}_D = 1.36$ is obtained with $\lambda/D_m = 2.5$ which is slightly lower than that of the wavy cylinder with $\lambda/D_m = 3$ and the circular cylinder. Increasing the Reynolds number to $Re = 100$, the minimum value of $\bar{C}_D$ is obtained with $\lambda/D_m = 2.5$. Compared with a circular cylinder, the lift fluctuation is significantly weakened for $\lambda/D_m = 2.0$ and 2.5, and the Strouhal numbers are lower. At $Re = 150$, the values of $\bar{C}_D$ for the wavy cylinders with $\lambda/D_m = 2.0$ and 2.5 are lower than that of the circular cylinder. However, the values of $\bar{C}_D$ are close to the values of a circular cylinder for $\lambda/D_m = 1.5$ and 3.0. In general, the optimal spanwise wavelength is slightly reduced with the increase in Reynolds numbers in the range $1.5 \leqslant \lambda/D_m \leqslant 3.0$. But it is still within the lower wavelength range $2.0 \leqslant \lambda/D_m \leqslant 2.5$. The spanwise vortex structures of the wavy cylinders ($\lambda/D_m = 2.0$ and 2.5, $a/D_m = 0.175$) at $Re = 80$ and 150 are shown in figure 14. Longer near wake vortex structures generated behind the wavy cylinder at $Re = 150$ contrast with the shorter vortex structures generated at $Re = 80$ for the wavy cylinder with $\lambda/D_m = 2$ and $a/D_m = 0.175$. A well-organized steady and symmetrical wavy vortex sheet structure is found for $\lambda/D_m = 2.5$ and $a/D_m = 0.175$ at $Re = 150$.

In the wavelength range $5.0 \leqslant \lambda/D_m \leqslant 7.5$, the value of optimal wavelength for $\bar{C}_D$ and C'_L reduction is also reduced with the increase in Reynolds numbers (see
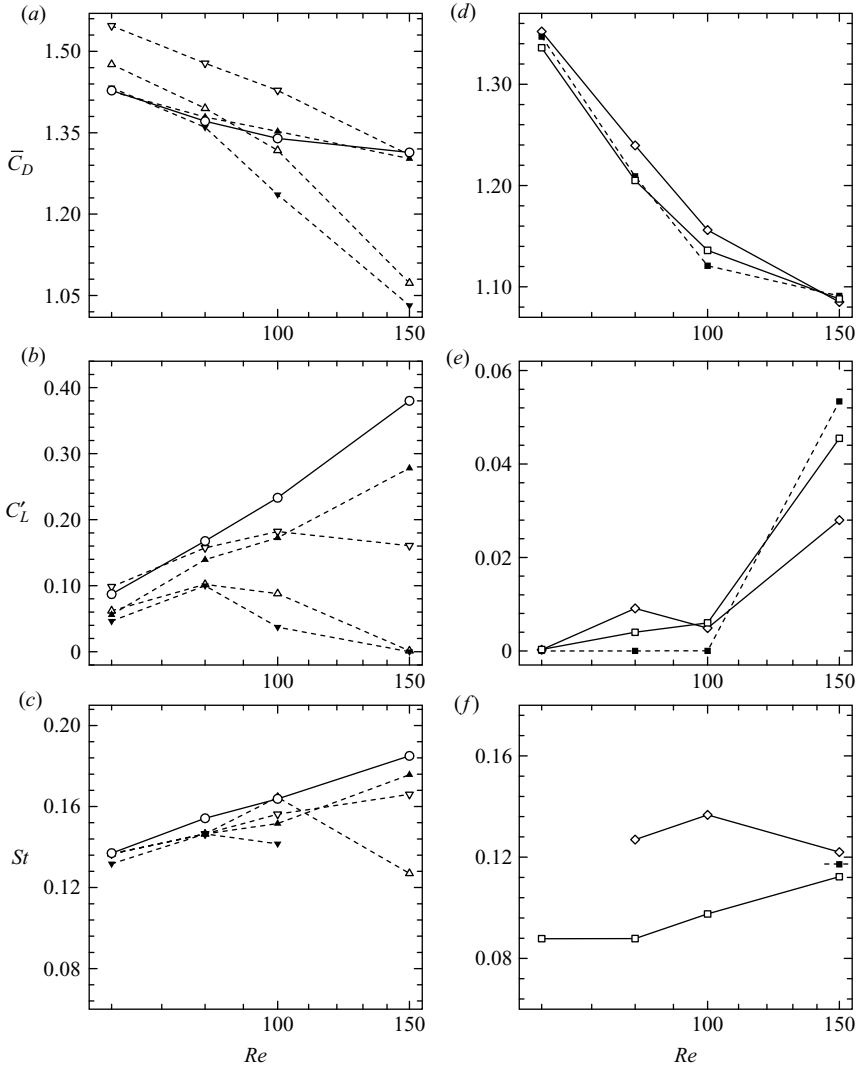
FIGURE 13. Mean drag coefficients, r.m.s. lift coefficients and Strohual numbers of wavy and circular cylinders at the Reynolds number values of 60–150: (a)–(c) $a/D_m = 0.175$ with —▽—, $\lambda/D_m = 1.5$; —△—, $\lambda/D_m = 2$; —▼—, $\lambda/D_m = 2.5$; —▲—, $\lambda/D_m = 3$; (d)–(f) $a/D_m = 0.15$ with —◇—, $\lambda/D_m = 5$; —■—, $\lambda/D_m = 6$; —□—, $\lambda/D_m = 7.5$; Here, —○—, circular cylinder.

figure 13d–f). The maximum drag reduction appears at $\lambda/D_m = 7.5$ for $Re = 60$, while it appears at $\lambda/D_m = 6$ for $Re = 100$. At $Re = 150$, the optimal value is further reduced to $\lambda/D_m = 5$. These phenomena are consistent with the results of Kim & Choi (2005), which used the active control method. As shown in figure 13(d), at $Re = 60$, 80 and 100, the drag reduction of a wavy cylinder with the optimal wavelength ($\lambda/D_m = 6$, $a/D_m = 0.15$) is 5.7 %, 11.8 % and 16.4 %, respectively, compared with that of a circular cylinder at the same Reynolds number. The magnitude of reduction decreases at $Re = 150$. The drag reduction is 17 % which is only slightly higher than that at $Re = 100$. The wake pattern of this wavy cylinder at $Re = 80$ and 100 is steady, and no vortex shedding appears (see figure 15a, b). At $Re = 150$, the wake vortex structure behind the wavy cylinder becomes unsteady, and the wake pattern reverts back to the vortex shedding characteristic (see figure 15c). The continuous distortion
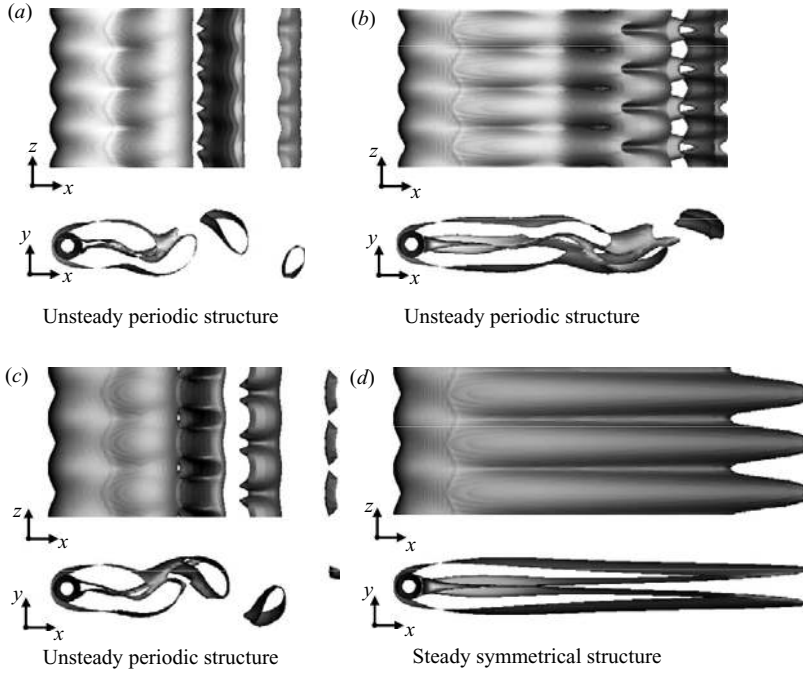
FIGURE 14. Instantaneous spanwise vortex structures for the wavy cylinders with $a/D_m = 0.175$: (a) $Re = 80$ ($\lambda/D_m = 2$); (b) $Re = 150$ ($\lambda/D_m = 2$); (c) $Re = 80$ ($\lambda/D_m = 2.5$); (d) $Re = 150$ ($\lambda/D_m = 2.5$).
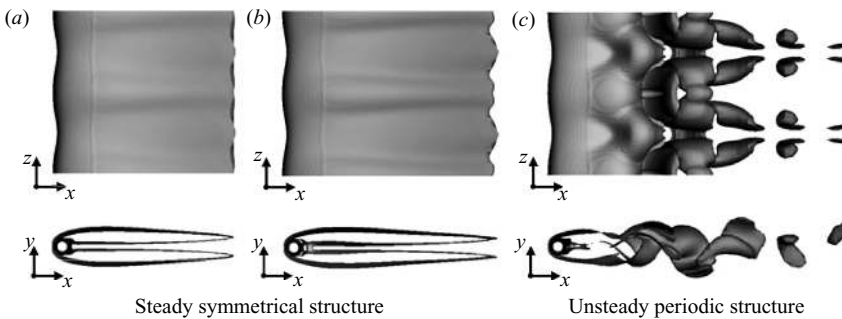

FIGURE 15. Instantaneous spanwise vortex structures for the wavy cylinder ($\lambda/D_m = 6$ and $a/D_m = 0.15$) at Reynolds number values of 40–150: (a) $Re = 80$; (b) $Re = 100$; (c) $Re = 150$.

of the vortex sheet leads to ultimate rolling up of three-dimensional vortex structure in the near wake with the occurrence of periodic vortex shedding at downstream position. This means that the effects of drag reduction and the suppression of r.m.s. lift still occur. Along the spanwise direction, the riblike vortex structures are formed. Figure 13(e, f) also confirms that the r.m.s. lift is discernible again and not fully suppressed for the wavy cylinder with $\lambda/D_m = 6$ and $a/D_m = 0.15$ at $Re = 150$. In the range $5.0 \leqslant \lambda/D_m \leqslant 7.5$ at $Re = 150$, all the wake patterns of the wavy cylinder become unsteady with three-dimensional vortex shedding at far downstream. From the discussion above, we can conclude that the vibration control by modifying the spanwise wavelength of the cylinder and the values of optimal wavelength are also Reynolds number dependent.

5. Conclusions

In the present investigations, the three-dimensional numerical simulations based on the finite volume method are used to calculate the laminar flow around wavy cylinders with different combinations of spanwise wavelength λ/D_m and wave amplitude a/D_m at low Reynolds numbers. The three-dimensional near wake vortex structures of wavy cylinders mainly at the Reynolds number of 100 were captured and analysed. It was found that such kind of wavy surfaces with certain optimal values of λ/D_m and a/D_m can significantly modify the free shear layer development and control the three-dimensional vortices formation behind the wavy cylinder. The wavy cylinders are classified into three wavelength regimes (I, II and III) with different flow patterns (A), (B) and (C). For flow pattern (A), the flow is unsteady and shows a quasi-two-dimensional unsteady wake structures similar to the straight circular cylinder. Flow pattern (B) is characterized by an increase of three-dimensional wake vortex distortion and vortex formation length with a progressive weakening of vortex shedding. In pattern (C), the flow pattern behind the wavy cylinder is very steady. A three-dimensional wavy vortex sheet is generated, but it does not roll up into a vortex even at far downstream position. The r.m.s. lift reduces to zero with the full suppression of vortex-induced vibration. The velocity separation line of the wavy cylinders varies along the spanwise direction. This leads to the distortion of the two-dimensional symmetrical vortex structures along the spanwise direction into three-dimensional structures. In regimes I and II with flow pattern (A) or (B), the wake width expands in the region behind the saddles of cylinders and shrinks behind the nodes of cylinders. On the contrary, in regimes II $\leftrightarrow$ III and III with the flow pattern (A) or (B), the wake width shrinks behind the saddle positions and expands at the nodal position. As a result, the near wake vortex structures exhibit a periodic variation along the spanwise direction. In both regimes with flow pattern (B), it is difficult for the free shear layer to roll up. Hence it can only develop into mature vortex at a further downstream position. A wavy cylinder with certain optimal values of λ/D_m and a/D_m can significantly modify and control the three-dimensional vortex structure behind itself. It weakens and even suppresses the vortex shedding. The base pressure coefficient decreases due to the formation of a longer vortex formation length. The mean drag coefficients of a typical wavy cylinder are reduced compared with those of a corresponding straight circular cylinder at the same Reynolds numbers. At an optimal wavelength λ/D_m around 6, the mean drag coefficient and the r.m.s. lift of a wavy cylinder drop sharply with the increase of wave amplitude a/D_m and the maximum drag coefficient reduction of up to 18 % is obtained. The reduction of the r.m.s. lift coefficients to zero indicates that such a wavy cylinder is an ideal device for the suppression of FIV. With a large value of wave amplitude, the three-dimensional near wake vortex structures are coherent and well organized. Furthermore, the value of optimal spanwise wavelength of the wavy cylinder for the control of FIV varies with the Reynolds number range 60–150. In the wavelength range $5.0 \leqslant \lambda/D_m \leqslant 7.5$, the value of optimal wavelength reduces from $\lambda/D_m = 6$ at $Re = 100$ to $\lambda/D_m = 5$ at $Re = 150$. In the wavelength regime $2.0 \leqslant \lambda/D_m \leqslant 2.5$, the variation of $\bar{C}_D$ and C'_L is small. The maximum drag reduction of up to 21.5 % is obtained at $Re = 150$ for $\lambda/D_m = 2.5$ and $a/D_m = 0.175$. In conclusion, the value of optimal wavelength decreases with the increase in Reynolds number.

Case	N_c	H/D_m (N_z)	Cells	$\Delta t U_\infty/D_m$	$\bar{C}_D$	C_L'	St	$-\bar{C}_{pb}$
CY-1	80	1 (16)	131200	0.025	1.3356	0.2285	0.1599	0.7246
CY-2	100	1 (16)	163200	0.025	1.3397	0.2342	0.1651	0.7259
CY-3	120	1 (16)	185600	0.025	1.3396	0.2337	0.1635	0.7292
CY-4a	120	3 (32)	371200	0.025	1.3396	0.2332	0.1638	0.7260
CY-4b	120	3 (32)	371200	0.0125	1.3406	0.2351	0.1643	0.7241
CY-5	120	6 (56)	649600	0.025	1.3391	0.2345	0.1645	0.7275
CY-6	140	1 (16)	208000	0.025	1.3405	0.2324	0.1636	0.7247
CY-7	160	1 (16)	243200	0.025	1.3414	0.2341	0.1644	0.7278

TABLE 3. Grid independence test of a circular cylinder at $Re = 100$: CY = circular cylinder; N_c = mesh numbers around the cylinder circumference; N_z = mesh layers along the cylinder spanwise direction.
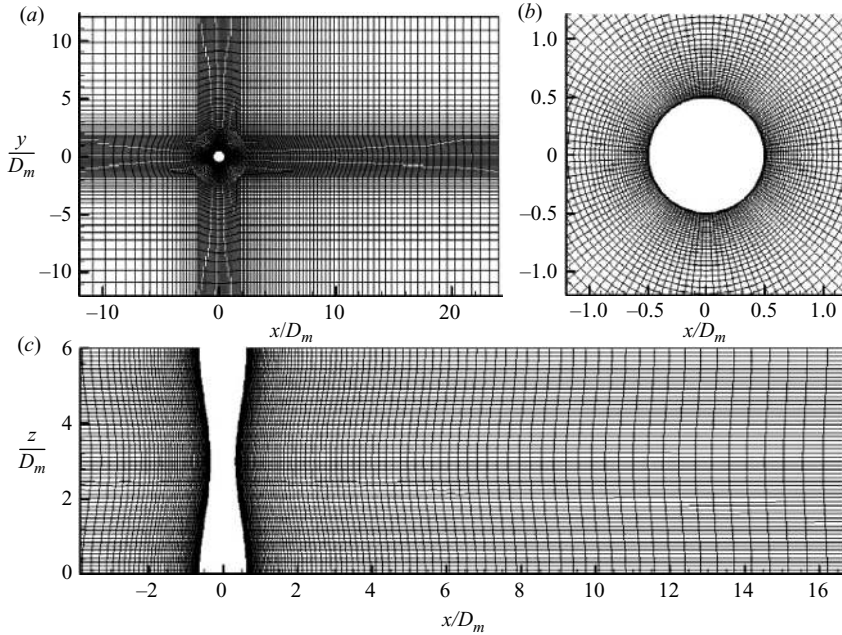

FIGURE 16. Computational domain and mesh distribution: (*a*) computational mesh distribution in the *x–y* plane; (*b*) mesh around the circumference of a cylinder; (*c*) spanwise direction mesh distribution.

Appendix. Grid independence test and the validation of numerical models

Grid independence test and the validation of numerical models are extremely important prior to extensive numerical simulations. Figure 16 shows the detailed diagram of the grid system. The mesh distribution in the *x–y* plane is non-uniform, while it is uniform along the *z*-direction (the spanwise direction of the cylinder). A finer grid was generated near the cylinder and gradually became coarser in the wake and the far field. The grid was clustered near the cylinder with an expansion rate of 1.2 in the radial direction from the cylinder surface.

Table 3 shows that seven circular cylinder mesh models were constructed for the present simulations at $Re = 100$. The distance between the first grid and the cylinder surface was $0.01D_m$. The dimensionless time steps $\Delta t U_\infty/D_m = 0.0125$ and 0.025 were

		$\bar{C}_D$				C_L'	St	$-\bar{C}_{pb}$
Authors	Re =	60	80	150	100	100	100	100
Past								
Williamson (1989)	Exp.	–	–	–	–	–	0.164	–
Henderson (1995)	Num.	1.42	1.37	1.34	1.35	–	–	0.73
Park, Kwon & Choi (1998)	Num.	–	1.35	–	1.33	0.23	0.165	0.74
Zhang *et al.* (1998)	Num.	–	–	–	1.32	0.23	–	–
Posdziech & Grundmann (2001)	Num.	1.39	1.35	1.32	1.33	–	–	–
Kim *et al.* (2005)	Num.	–	1.36	–	1.34	0.23	–	0.72
Sharman *et al.* (2005)	Num.	–	–	–	1.33	0.23	0.164	0.72
Present								
CY-4a	Num.	1.43	1.37	1.32	1.34	0.23	0.164	0.73

TABLE 4. Comparison with published results for circular cylinder.

used. At each time step, when the sum of absolute mass imbalance over all the mesh elements decreased to 0.0001 of the total mass flux across the inlet section, the iteration was deemed to be convergent. With different grid numbers, grid independence tests were satisfied if the variation in the values of $\bar{C}_D$, C_L', St and $-\bar{C}_{pb}$ were all very small. The wake vortex structures were also very similar. Moreover, the two different time steps $\Delta t U_\infty / D_m$ (see table 3; CY-4a and CY-4b) had negligible effect on the values above. Because of the two-dimensional steady characteristic of flow around a circular cylinder at $Re = 100$, the computational domain height (H/D_m) also had no effect on the different parameters. Hence, it can be said with confidence that the grid size used in the present study is sufficiently accurate to simulate the laminar flow around the cylindrical bluff bodies. As shown in table 4, the values of $\bar{C}_D$, C_L', St and $-\bar{C}_{pb}$ of the present simulations (case CY-4a) are all in good agreement with other published results of a circular cylinder by Williamson (1989), Henderson (1995), Park, Kwon & Choi (1998), Zhang & Dalton (1998), Posdziech & Grundmann (2001), Kim & Choi (2005) and Sharman *et al.* (2005) at $Re = 60$, 80, 100 and 150, respectively. Moreover, figure 17 shows the grid independence tests for several wavy cylinders with different cell numbers and time steps at $Re = 100$. No notable discrepancy of $\bar{C}_D$ and C_L' in the same wavy cylinder by adopting different circumference mesh numbers (N_c), spanwise mesh layers (N_z) and different time steps were found.

Based on these analyses, the mesh model with cell numbers of 11 600 in the x–y plane for both circular and wavy cylinders was adopted for capturing detailed vortex structures and concurrently saving the computational time. The zone close to the cylinder surface was meshed with 120 grids ($N_c = 120$) uniformly distributed along the circumferential direction. On the other hand, uniform grid layers of 16–88 were respectively used in the spanwise direction for λ/D_m ranging from 1 to 10 (figure 16). For all of the present simulations, a constant non-dimensional time step is used with $\Delta t U_\infty / D_m = 0.025$.

By adopting periodic boundary conditions, the computational domain height (H/D_m) was equal to one wavelength λ of a wavy cylinder. To validate the accuracy of the present periodic boundary conditions with only one wavelength λ in the computational domain, tests were also performed for some typical wavy cylinders with two ($\lambda/D_m = 3$, $a/D_m = 0.25$; $\lambda/D_m = 6$, $a/D_m = 0.15$; $\lambda/D_m = 9$, $a/D_m = 0.1$) and three ($\lambda/D_m = 2$, $a/D_m = 0.1$; $\lambda/D_m = 2$, $a/D_m = 0.25$; $\lambda/D_m = 6$, $a/D_m = 0.15$) wavelengths at $Re = 100$. No differences in forces, velocity distributions and wake
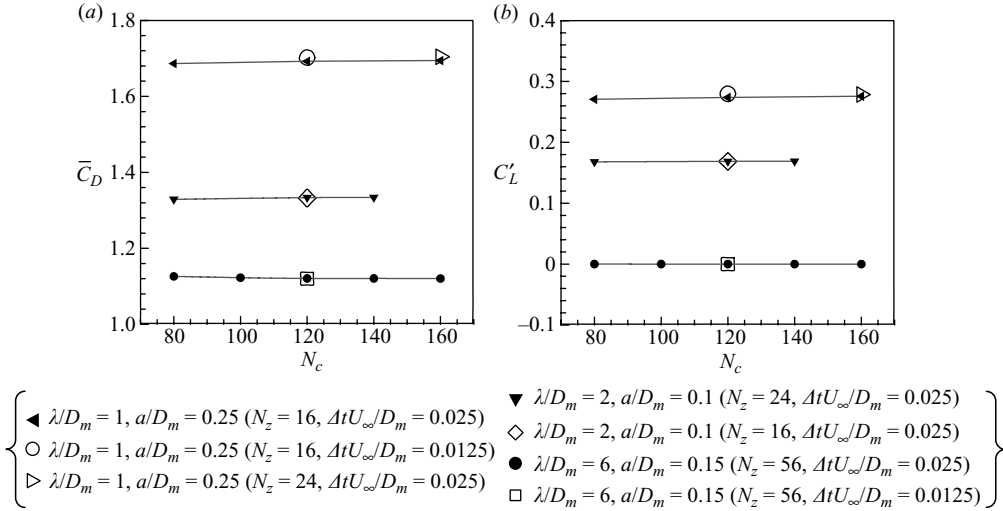
FIGURE 17. Grid independence test for different wavy cylinders at $Re = 100$.

topologies were obtained. Similar validation test with only one wavelength height in the computational domain was also discussed by Darekar & Sherwin (2001b) who numerically investigated the flow past a square cylinder with a wavy stagnation face at the Reynolds number equal to 100. Kim & Choi (2005) also found that doubling the computational spanwise height to 2λ did not cause any changes in the flow structure and the force values by using an active open-loop control method for reduction of drag of a circular cylinder at the Reynolds number less than 140.

REFERENCES

AHMED, A. & BAYS-MUCHMORE, B. 1992 Transverse flow over a wavy cylinder. *Phys. Fluids* A **4**, 1959–1967.

AHMED, A., KHAN, M. J. & BAYS-MUCHMORE, B. 1993 Experimental investigation of a three-dimensional bluff-body wake. *AIAA J.* **31**, 559–563.

BEARMAN, P. W. & OWEN, J. C. 1998 Reduction of bluff-body drag and suppression of vortex shedding by the introduction of wavy separation lines. *J. Fluids Struct.* **12**, 123–130.

DAREKAR, R. M. & SHERWIN, S. J. 2001*a* Flow past a bluff body with a wavy stagnation face. *J. Fluids Struct.* **15**, 587–596.

DAREKAR, R. M. & SHERWIN, S. J. 2001*b* Flow past a square-section cylinder with a wavy stagnation face. *J. Fluid Mech.* **426**, 263–295.

DOBRE, A., HANGAN, H. & VICKERY, B. J. 2006 Wake control based on spanwise sinusoidal perturbations. *AIAA J.* **44**, 485–492.

HENDERSON, R. D., 1995 Details of the drag curve near the onset of vortex shedding. *Phys. Fluids* **7**, 2102–2104.

KESER, H. IBRAHIM, ÜNAL, M. FEVZI & BEARMAN, P. W. 2001 Simulation of wake from a circular cylinder withspanwise sinusoidal waviness. *Proc. Second Intl Conf. Vortex Methods*, Istanbul, Turkey, (ed. M. Fevzi Ünal) September 26–28, 2001, 131–137.

KIM, J. & CHOI, H. 2005 Distributed forcing of flow over a circular cylinder. *Phys. Fluids* **17**, 033103.

KIM, J., HAHN, S., KIM, J., LEE, D., CHOI, J., JEON, W.-P. & CHOI, H. 2004 Active control of turbulence flow over a model vehicle for drag reduction. *J. Turbulence* **5**, 019.

LAM, K. & LIN, Y. F. 2007 Drag force control of flow over wavy cylinders at low Reynolds number. *J. Mech. Sci. Technol.* **21**, 1331–1337.

LAM, K. & LIN, Y. F. 2008 Large eddy simulation of flow around wavy cylinders at a subcritical Reynolds number. *Intl J. Heat Fluid Flow* **29**, 1071–1088.

LAM, K., WANG, F. H., LI, J. Y. & SO, R. M. C. 2004*a* Experimental investigation of the mean and fluctuating forces of wavy (varicose) cylinders in a cross-flow. *J. Fluids Struct.* **19**, 321–334.

LAM, K., WANG, F. H. & SO, R. M. C. 2004*b* Three-dimensional nature of vortices in the near wake of a wavy cylinder. *J. Fluids Struct.* **19**, 815–833.

LEE, S. J. & NGUYEN, A. T. 2007 Experimental investigation on wake behind a wavy cylinder having sinusoidal cross-sectional area variation. *Fluid Dyn. Res.* **39**, 292–304.

OWEN, J. C., SZEWCZYK, A. A. & BEARMAN, P. W. 2000 Suppression of Kármán vortex shedding. *Phys. Fluids* **12**, S9.

PARK, J., KWON, K. & CHOI, H. 1998 Numerical solutions of flow past a circular cylinder at Reynolds number up to 160. *KSME Intl J.* **12**, 1200–1205.

POSDZIECH, O. & GRUNDMANN, R. 2001 Numerical simulation of the flow around an infinitely long circular cylinder in the transition regime. *Theoret. Comput. Fluid Dyn.* **15**, 121–141.

SHARMAN, B., LIEN, F. S., DAVIDSON, L. & NORBERG, C. 2005 Numerical predictions of low Reynolds number flows over two tandem circular cylinders. *Intl J. Numer. Meth. Fluids* **47**, 423–447.

TOMBAZIS, B. & BEARMAN, P. W. 1997 A study of three-dimensional aspects of vortex shedding from a bluff body with a mild geometric disturbance. *J. Fluid Mech.* **330**, 85–112.

WILLIAMSON, C. H. K. 1989 Oblique and parallel modes of vortex shedding in the wake of a circular cylinder at low Reynolds numbers. *J. Fluid Mech.* **206**, 579–627.

ZHANG, J. F. & DALTON, C. 1998 A three-dimensional simulation of a steady approach flow past a circular cylinder at low Reynolds number. *Intl J. Numer. Meth. Fluids* **26**, 1003–1022.

ZHANG, W., DAI, C. & LEE, S. J. 2005 PIV measurements of the near-wake behind a sinusoidal cylinder. *Exps. Fluids* **38**, 824–832.